Title	Effect of annual rings on transmission of 100 GHz millimeter waves through wood
Author(s)	Tanaka, Soichi; Fujiwara, Yuko; Fujii, Yoshihisa; Okumura, Shogo; Togo, Hiroyoshi; Kukutsu, Naoya; Mochizuki, Shoji
Citation	Journal of Wood Science (2013), 59(5): 375-382
Issue Date	2013-10
URL	http://hdl.handle.net/2433/193011
Right	The final publication is available at Springer via http://dx.doi.org/10.1007/s10086-013-1342-6.
Type	Journal Article
Textversion	author

Original article

Title
Effect of annual rings on transmission of 100 GHz millimeter waves through wood*

Author's information
Soichi Tanaka, Yuko Fujiwara, Yoshihisa Fujii, Shogo Okumura
Graduate School of Agriculture, Kyoto University, Kyoto 606-8502, Japan

Hiroyoshi Togo, Naoya Kukutsu
NTT Microsystem Integration Laboratories, Atsugi 243-0198, Japan

and

Shoji Mochizuki
NTT Access Network Service Systems Laboratories, Tsukuba 305-0805, Japan

Corresponding Author
Soichi Tanaka
e-mail: stanaka@h3news1.kais.kyoto-u.ac.jp
Tel. +81-75-753-6245; Fax. +81-75-753-6245

Keywords
Millimeter wave, 100 GHz, NDE, Annual rings, Diffraction

* Part of this report was presented at the 61nd Annual Meeting of the Japan Wood Research Society, Kyoto, March 2011.

Abstract

For the application of millimeter wave (MMW) technique to non-destructive evaluation of wood, the effect of annual rings on the behavior of a 100 GHz MMW transmitted through wood was examined. The complex amplitude was measured for 2 mm thick flat- (LT) and quarter-sawn (LR) specimens of several species with different annual ring structures at 11% moisture content, of which the density distribution was measured using X-ray radiography. For the LT specimens of all species and the LR specimens with small density fluctuation or with earlywood width smaller than the wavelength of the MMW (= 3 mm), the amplitude and phase of the transmitted wave were similar to those of the wave without a specimen. For the LR specimen with large density fluctuation and with earlywood width close to or larger than the wavelength, the amplitude and phase were different from those of the wave without a specimen. All the measured complex amplitudes were well expressed using a diffraction model. It was concluded that the MMW is deformed by the density distribution and then its components with periods shorter than the wavelength by diffraction are attenuated.

Introduction

Wood is widely used in industrial products such as furniture and structural members. The constant use of wood in industry, however, has been sometimes disturbed by the fluctuation of physical properties in wood because this fluctuation may cause defects in the wood products. For example, the abrupt change of wood density causes the structural defects such as raised and loosened grains. Thus, the physical properties should be evaluated nondestructively in order to control the quality of the wood products [1].

A millimeter wave (MMW) technique, which deals with electromagnetic waves in the 30 to 300 GHz frequency range, has considerable promise as a tool for the nondestructive evaluation (NDE) of the wood products, because it is inexpensive, non-contact, non-invasive, and compact. Recent studies have shown that this technique can obtain the transmission image of wood [2, 3] with higher spatial resolution than the conventional microwave technique in the 3 to 30 GHz frequency range [4–13]. However, the image presented no quantitative physical property of wood, because the effect of wood structure on the MMW transmission through wood was obscure.

The transmitted waves are probably affected by micro- and macrostructures [14]. The microstructure can be regarded as homogeneous because wood cells, such as the tracheids, fibers, and ray cells, have cross-sectional dimensions much smaller than the wavelength of the MMWs, 1 to 10 mm. The macrostructure such as annual rings can be regarded as inhomogeneous because annual ring widths are close to or longer than the wavelength.

The effect of the microstructure on the MMW transmission has been explained by dielectric properties of wood [15]. On the other hand, little attention has been paid to the effect of the macrostructure such as annual rings. The understanding of this effect may improve the measurement accuracy of the physical properties of wood.

The purpose of this study was to examine the effect of annual rings on the behavior of the MMWs transmitted through 2 mm thick flat- and quarter-sawn specimens of softwood and ring- and diffuse-porous hardwood species. The complex amplitude of the transmitted wave was measured using linear scanning and discussed based on a model in consideration of both the micro- and macrostructures.

Theory

Macrostructure such as the annual rings is formed by the aggregation of microstructure such as the wood cells. Thus, in this study the effect of the macrostructure on the MMWs is treated as the distribution of the effect of the microstructure on them.

When a MMW is transmitted through a wood specimen, it will be locally affected by the complex permittivity due to the microstructure and be diffracted in the specimen simultaneously. However, it is difficult to build a model for such a phenomenon. Let us consider that the diffraction starts at the plane which is perpendicular to the wave propagation direction and includes the center of the specimen in the direction, while the wave is affected by the local complex permittivity in all the position in the specimen. Thus, it can be assumed in a right-handed Cartesian coordinate system (x, y, z) that a wave is rectilinearly propagated through a specimen in the z direction while being locally affected by its complex permittivity and is subsequently diffracted in free space at a distance of half the optical length of the specimen along the z-axis in the specimen and at a distance of l_0 (= 1 mm) in air (Fig. 1) if the double counting of the phase was corrected. The wave was assumed to be polarized constantly and linearly in the y direction, to illuminate perpendicularly to the specimen whose longitudinal direction is in the y direction (Fig. 1), and to be expressed as a complex amplitude. The complex permittivity of the specimen in the longitudinal direction was assumed to be constant along the z-axis and represented by $\varepsilon(x, y)$.

The complex amplitude of the wave propagated rectilinearly through the specimen is formulated as follows [16, 17]:

$$f(x,y) = S_{21}(x,y)V_{\mathrm{i}}(x,y), \tag{1}$$

where $V_{\mathrm{i}}(x, y)$ represents the complex amplitude of the incident wave and $S_{21}(x, y)$ the S-parameter which is formulated as follows:

$$\begin{gathered} S_{21}(x,y) = \frac{1-\{R(x,y)\}^2}{1-R(x,y)\Lambda(x,y)}\Lambda(x,y), \\ \left(\begin{array}{l} R(x,y) = \dfrac{1-\sqrt{\varepsilon(x,y)}}{1+\sqrt{\varepsilon(x,y)}}, \\ \Lambda(x,y) = \exp\left\{\mathrm{i}2\pi(\sqrt{\varepsilon(x,y)}-1)d/\lambda\right\} \end{array} \right) \end{gathered} \tag{2}$$

where d represents the specimen thickness (= 2 mm), and λ the wavelength of the MMW in air (= 3 mm).

The diffraction of the waves in free space is explained by Fourier optics [18], in which the complex amplitude of a diffracted wave at output xy-plane is related to that of a wave at input xy-plane using a transfer function. When the complex amplitude of the wave at input xy-plane is equal to $f(x, y)$ (Fig. 1), that of the diffracted wave, $g(x, y)$, can be formulated as follows:

$$g(x,y) = \exp(-\mathrm{i}2\pi l/\lambda)\int_{-\infty}^{\infty}\int_{-\infty}^{\infty} H(v_x,v_y)F(v_x,v_y)\exp\left\{\mathrm{i}2\pi(v_x x + v_y y)\right\}\mathrm{d}v_x\mathrm{d}v_y, \tag{3}$$

where v_x and v_y represent the spatial frequencies in the x and y directions, respectively, $\exp(-\mathrm{i}2\pi l/\lambda)$ represents the factor which prevents the double counting of the phase, and $F(v_x, v_y)$, $H(v_x, v_y)$, and l represent the Fourier transformation, transfer function of $f(x, y)$, and the optical length between input and output planes, respectively, which are formulated as follows:

$$F(v_x,v_y) = \int_{-\infty}^{\infty}\int_{-\infty}^{\infty} f(x,y)\exp\left\{-\mathrm{i}2\pi(v_x x + v_y y)\right\}\mathrm{d}x\mathrm{d}y, \tag{4}$$

$$H(v_x,v_y) = \exp\left\{\mathrm{i}2\pi\left(\frac{1}{\lambda^2} - v_x^2 - v_y^2\right)^{\frac{1}{2}} l\right\}, \tag{5}$$

$$l = l_0 + \frac{d\,\mathrm{Re}\sqrt{\bar{\varepsilon}}}{2}, \tag{6}$$

where $\bar{\varepsilon}$ represents the average complex permittivity of the specimen,

$$\bar{\varepsilon} = \frac{\int_{-\infty}^{\infty}\int_{-\infty}^{\infty}\varepsilon(x,y)\mathrm{d}x\mathrm{d}y}{\int_{-\infty}^{\infty}\int_{-\infty}^{\infty}\mathrm{d}x\mathrm{d}y}. \tag{7}$$

Equations (1) to (7) define a diffraction model in this study and are summarized as follows:

1. The incident wave is deformed by the complex permittivity distribution (Eqs. (1) and (2)).
2. The diffraction attenuates the deformed wave components with periods shorter than the wavelength, λ (Eqs. (3) to (7)), because the transfer function $H(v_x, v_y)$ acts as an attenuator if the spatial period of $f(x, y)$, $(v_x^2 + v_y^2)^{-1/2}$, is less than λ.

Experimental set-up

Specimens

Flat- (large surface parallel to LT plane, LT) and quarter-sawn (LR) specimens, 100 mm square and 2 mm thick, were prepared from sound wood of softwoods, hinoki (*Chamaecyparis obtusa*), sugi (*Cryptomeria japonica*), and akamatsu (*Pinus densiflora*); ring-porous hardwoods, kiri (*Paulownia tomentosa*) and keyaki (*Zelkova serrata*); and diffuse-porous hardwood, tochinoki (*Aesculus turbinata*). The specimens were stored over a saturated NaBr solution in desiccators at 27.5 °C until their moisture content reached 11%. A Cartesian coordinate system (x, y, z) was defined on the specimen with its larger surface parallel to the xy-plane and its center on the z-axis.

Density measurement with X-ray radiography

The density of specimens was measured using X-ray radiography. Figure 2 shows an experimental set-up for X-ray radiography using an X-ray television inspection equipment (FI-30, Shimadzu). The X-rays were generated by an X-ray tube at a tube voltage and current of 32 kV and 1.0 mA, respectively. The rays that passed through the specimen were converted into a visible image by an image intensifier (I.I.). The image was captured by a CCD camera (640×480 pixel, 256 gray levels) and sent to a computer in order to obtain the intensity of the rays, $I(X, Y)$, in a Cartesian coordinate system (X, Y), where X and Y are in the width and height directions of the image, respectively (Fig. 2). The specimen was set so that its center was at (X, Y) = (320, 240) and its longitudinal direction was parallel to the Y-axis.

The intensity of the rays that passed through the specimen at (X, Y) is formulated as follows:

$$I(X,Y) = I_0(X,Y)\exp\{-\mu\rho(X,Y)d\}, \tag{8}$$

where $I_0(X, Y)$ represents intensity of the rays at (X, Y) without a specimen, $\rho(X, Y)$ the air-dry density of the specimen averaged along the z-axis, and μ the mass attenuation coefficient. Assuming that μ is constant for all the specimens, Eq. (8) can be transformed into:

$$\Gamma = -\mu\rho_a d\,, \tag{9}$$

where Γ and ρ_a represent the averages of the logarithmic intensity attenuation and air-dry density over the coverage area of the image, respectively, and they are expressed using discrete values for each pixel as follows:

$$\Gamma = \frac{\sum_{X=1}^{640}\sum_{Y=1}^{480}\ln\dfrac{I(X,Y)}{I_0(X,Y)}}{640\cdot 480}, \tag{10}$$

$$\rho_a = \frac{\sum_{X=1}^{640}\sum_{Y=1}^{480}\rho(X,Y)}{640\cdot 480}. \tag{11}$$

The relation of the average attenuation, Γ, to the product of the average air-dry density and the thickness, $\rho_a d$, was obtained for all specimens in a preliminary experiment (Fig. 3). There was a good linear relation between them, and the mass attenuation, μ, was determined to be 0.4640 cm^2/g using Eq. (9) from the slope of the regression line.

The density of a specimen, $\rho(X, Y)$, was estimated using Eq. (8) for 640 × 480 pixel points and resampled to $\rho(x, y)$ with 1024 ×1024 pixels over an area of –24 mm ≤ x ≤ 24 mm and –20 mm ≤ y ≤ 20 mm by Shepard's method [19] using the X-ray image of a square mesh of 0.35 mm thick steel wires with 5 mm spacing in order to perform a fast Fourier transform (FFT) and an inverse FFT (IFFT) in the discussion described below. Furthermore, an oven-dry density, $\rho_0(x, y)$, was obtained from the air-dry one, $\rho(x, y)$, using the equation, $\rho = 1.11\rho_0/(1 + 0.094\rho_0)$, for wood at 11% MC [20].

Oven-dry density, $\rho_0(x, y)$, obtained in this way is shown in Figs. 4 and 5 as grayscale images for the LT

and LR specimens, respectively. The LT specimens showed smooth tones of gray (Fig. 4), while the LR specimens showed remarkable stripped patterns due to the annual rings (Fig. 5).

The complex permittivity in the longitudinal direction of wood at 11% MC, $\varepsilon(x, y)$, was determined as follows:

$$\varepsilon(x,y) = 1 + \frac{0.760(\varepsilon_{WS} - 1)\rho_0(x,y)}{1 + 0.094\rho_0(x,y)}. \tag{12}$$

This equation was derived from a parallel capacitor formula, $\varepsilon = 1 - v_{WS} + v_{WS}\varepsilon_{WS}$ [21, 22], where ε_{WS} represents complex permittivity of wood substance and v_{WS} volume fraction of wood substance which was expressed as $0.760\rho_0/(1 + 0.094\rho_0)$ at 11% MC [23]. In an experiment described in another article submitted to this journal, Eq. (12) was confirmed to be well fitted to the complex permittivity in the longitudinal direction for LT specimens of nine wood species at 11% MC measured using a free space method in the range of ρ_0 = 0.2–1.0 g/cm^3 and the complex value of ε_{WS} was estimated to be 4.1 (1 + 0.12 i).

Apparatus and measurement

Figure 6 shows an experimental set-up of a MMW measurement system arranged in a right-handed Cartesian coordinate system (x, y, z). A MMW signal of 100 GHz with an average output power of 10 mW was oscillated in a Gunn diode and divided into two signals, measurement and reference, by a directional coupler. The reference signal was sent to an in-phase/quadrature mixer (IQ-mixer) through a dielectric waveguide. The measurement signal was modulated using a PIN diode at a switching frequency of 100 kHz and passed through a phase shifter. The wave linearly polarized in the y direction was transmitted by a conical horn antenna towards the z direction, and collimated using a Teflon plano-parabolic lens with a diameter of 80 mm and a focal length of 33 mm. The wave that passed through the specimen was received by an open-ended rectangular waveguide with an inner cross section of 2.54 mm in the x direction and 1.27 mm in the y direction and sent to the IQ-mixer, where the in-phase (I) and quadrature (Q) components were discriminated by comparing the measurement and reference signals. The signals from the IQ-mixer were processed into the voltages, V_I and V_Q, in a lock-in amplifier. The front face of the waveguide, excluding the aperture, was covered with MMW absorbent material to prevent reflections from the waveguide and surrounding apparatuses.

The complex amplitude of the MMW was determined as:

$$V = V_I + \mathrm{i}\left(\frac{V_I}{\tan(\xi_Q - \xi_I)} - \frac{V_Q}{(A_Q/A_I)\sin(\xi_Q - \xi_I)}\right), \tag{13}$$

where A_I, A_Q and ξ_I, ξ_Q are the amplitude and phase of the sinusoidal functions obtained as the regression lines of the relation between V_I, V_Q and the phase controlled by the phase shifter and were determined in a preliminary experiment.

The waveguide was set at (y, z) = (0, 113 mm) and moved along the x-axis in steps of 1 mm within a range of –20 mm $\le x \le$ 20 mm for line scanning with and without a specimen (Fig. 6). Furthermore, it was set at z = 110 mm for area scanning of an incident wave (–24 mm $\le x \le$ 24 mm and –20 mm $\le y \le$ 20 mm, 1 mm step along the x- and y-axes) (Fig. 6).

Figures 7 (a) and (b) show the distributions of the amplitude, $|V_i(x, y)|$, and phase, $\arg V_i(x, y)$, of the incident MMW at z = 110 mm. Fig. 7 (a) shows a bright region in the center and concentric bright rings around it, so called main lobe and side lobes, respectively [24–27]. In Fig. 7 (b), there are three concentric regions, gray, dark gray, and black, corresponding to one main and two side lobes. These distributions were obtained over the area of –24 mm $\le x \le$ 24 mm and –20 mm $\le y \le$ 20 mm with 49 × 41 pixels. To perform the FFT and IFFT in the discussion described below, they were resampled to the distributions with 1024 × 1024 pixels using Shepard's method [19], and the complex amplitude, $V_i(x, y)$, was obtained.

Figure 7 (c) shows the distributions of the amplitude, $|V_0|$, and phase, $\arg V_0$, of the MMW without a specimen along x-axis at (y, z) = (0, 113 mm). The distribution, $|V_0|$, has a large peak in center and two small peaks near either end, and $\arg V_0$ has three plateau regions in the range of – 12 mm $\le x \le$ 12 mm, – 20 mm $\le x \le$ – 15 mm, and 15 mm $\le x \le$ 20 mm, corresponding to one main and two side lobes.

Results and discussion

The amplitude, $|V|$, and phase, $\arg V$, of the transmitted MMWs measured along x-axis at (y, z) = (0, 113 mm) are shown in Figs. 8 and 9 for the LT and LR specimens, respectively. For the LT specimens of all species (Fig. 8) and LR specimens of hinoki, keyaki, and tochinoki (Fig. 9(a), (e), and (f)), the variation patterns of $|V|$ and $\arg V$ were similar to those of $|V_0|$ and $\arg V_0$ in Fig. 7(c), though $|V|$ was slightly attenuated in comparison with $|V_0|$ and $\arg V$ was shifted away from $\arg V_0$ towards the positive direction. For the LR specimens of sugi, akamatsu, and kiri (Fig. 9(b), (c), and (d)), on the other hand, the patterns of $|V|$ and $\arg V$ were different from those in $|V_0|$ and $\arg V_0$ (Fig. 7(c)).

The complex amplitude of a diffraction model, $g(x, y)$, was estimated for z = 113 mm by substituting the interpolated complexes, $V_i(x, y)$ and $\rho_0(x, y)$, for Eqs. (1) to (7) and (12), of which Eqs. (3), (4), and (7) were computed using the IFFT, FFT, and numerical integration, respectively, in a discrete-finite form. In consideration of the aperture area of the receiving waveguide in Fig. 6, the simple moving averaged complex amplitude, $g_s(x, y)$, was calculated as simple moving averages of $g(x, y)$ over 2.54 mm in the x direction and 1.27 mm in the y direction. The amplitude, $|g_s(x)|$, and phase, $\arg g_s(x)$, estimated from the diffraction model are shown as solid and dotted lines, respectively, in Figs. 8 and 9. The plots, $|V|$ and $\arg V$, for all the specimens matched well the lines estimated from the model (Figs. 8 and 9). This indicates that the diffraction model is valid for MMWs transmitted through wood specimen and that the waves may be deformed by the complex permittivity distribution due to the density distribution as shown in Figs. 4 and 5 and then their components with periods shorter than the wavelength of the MMWs, λ (= 3 mm), must be attenuated.

The LT specimens of all species and LR specimens of hinoki, keyaki, and tochinoki had small density fluctuations in the xy-plane or earlywood widths smaller than λ (Figs. 4 and 5(a), (e), and (f)), while the LR specimens of sugi, akamatsu, and kiri had large density fluctuations in the xy-plane and earlywood widths close to or larger than λ (Fig. 5(b), (c), and (d)). This is why the amplitude and phase of the transmitted wave for LR specimens of sugi, akamatsu, and kiri were different from those of the wave without a specimen on the basis of the diffraction model.

Conclusion

The complex amplitude was measured for 2 mm thick flat- (LT) and quarter-sawn (LR) wood specimens with different annual ring structures, of which the density distribution was measured using X-ray radiography. For the LT specimens of all species and the LR specimens with small density fluctuation or with earlywood width smaller than the wavelength of the MMWs, λ (= 3 mm), the amplitude and phase of the transmitted wave were similar to those of the wave without a specimen. For the LR specimen with large density fluctuation along its large surface and with earlywood width close to or larger than λ, the amplitude and phase were different from those of the wave without a specimen. All the measured complex amplitudes were well expressed using a diffraction model. It was concluded from these findings that the incident wave is deformed by the density distribution and then its components with periods shorter than λ by the diffraction are attenuated. Furthermore, these findings will not only improve the measurement accuracy of the physical properties of wood but also provide a new technique such as the detection of the annual rings without scanning. Further study is necessary to examine these effects for the specimens whose large surfaces are not parallel to LT and LR planes.

Acknowledgements

This work was supported in part by a Grant-in-Aid from Japan Society for the Promotion of Science for JSPS Fellows (233453) and in part by a Grant-in-Aid from JSPS (21300329). The authors would like to express their appreciation to Professor Dr. Tadao Nagatsuma of the Graduate School of Engineering Science, Osaka University, who gave us advise on how to adjust the measurement system.

Reference

1. Beall FC (2000) Subsurface sensing of properties and defects in wood and wood products. Subsurf Sens Tech Appl 1:181–204
2. Laurinavičius A, Baltrušaitis A, Pranckevičiene V, Ukvalbergienė K (2010) Wood characterization by scanning millimeter wave beam. ISSN 1392–1320 Mater Sci (Medžiagotyra)16:63–66
3. Oyama Y, Zhen L, Tanabe T, Kagaya M (2009) Sub-terahertz imaging of defects in building blocks. NDT & E Int 42:28–33
4. Hansson L, Lundgren N, Antti AL, Hagman O (2005) Microwave penetration in wood using imaging sensor. Meas 38:15–20
5. James WL, Yen Y-H, King RJ (1985) A microwave method for measuring moisture content, density, and grain angle of wood. Research note FPL-0250
6. Johansson J, Hagman O, Fjellner B-A (2003) Predicting moisture content and density distribution of Scots pine by microwave scanning of sawn timber. J Wood Sci 49:312–316
7. King RJ, Yen YH (1981) Probing Amplitude, Phase, and Polarization of Microwave Field Distributions in Real Time. IEEE Trans Micro Theory Tech 29:1225–1231
8. Lundgren N, Hagman O, Johansson J (2006) Predicting moisture content and density distribution of Scots pine by microwave scanning of sawn timber II: evaluation of models generated on a pixel level. J Wood Sci 52:39–43
9. Martin P, Collet R, Barthelemy P, Roussy G (1987) Evaluation of wood characteristics: Internal scanning of the material by microwaves. Wood Sci Technol 21:361–371
10. Portala J-F, Ciccotelli J (1992) Nondestructive testing techniques applied to wood scanning. Ind Metrol 2:299–307
11. Schajer GS, Orhan FB (2005) Microwave Non-Destructive Testing of Wood and Similar Orthotropic Materials. Subsurface Sensing Technologies and Applications 6:293–313
12. Schajer GS, Orhan FB (2006) Measurement of wood grain angle, moisture content and density using microwaves. Holz als Roh- und Werkstoff 64:483–490
13. Shen J, Schajer G, Parker R (1994) Theory and practice in measuring wood grain angle using microwaves. IEEE Trans Instrum Meas 43:803–809
14. Bucur V (2003) Nondestructive characterization and imaging of wood. Springer, Berlin, pp 1–354
15. Tanaka S, Fujiwara Y, Fujii Y, Okumura S, Togo H, Kukutsu N, Nagatsuma T (2011) Effect of grain direction on transmittance of 100-GHz millimeter wave for hinoki (Chamaecyparis Obtusa). J Wood Sci 57:189–194
16. Ghodgaonkar DK, Varadan VV, Varadan VK (1989) A Free-Space Method for Measurement of Dielectric Constants and Loss Tangents at Microwave Frequencies. IEEE Trans Instr Meas 37:789–793
17. Ghodgaonkar DK, Varadan VV, Varadan VK (1990) Free-Space Measurement of Complex Permittivity and Complex Permeability of Magnetic Materials at Microwave Frequencies. IEEE Trans Instr Meas 39:387–394
18. Saleh BEA, Teich MC (1991) Fundamentals of photonics. John Wiley & Sons, Inc, New York, pp108–156
19. Shepard D (1968) A two-dimensional interpolating function for irregularly spaced data. Proc ACM 23rd Nat Conf pp517–524
20. Kollmann F (1951) Technologie des Holzes und Der Holzwerkstoffe 1, Springer, Berlin, pp1–1050
21. Kröner K, Pungs L (1952) Zur dielektrischen Anisotropie des Naturholzes im großen Frequenzbereich. Holzforschung 6:13–16
22. Kröner K, Pungs L (1953) Über das Verhalten des dielektrischen Verlustfaktors des Naturholzes im großen Frequenzbereich. Holzforschung 7:12–18
23. Uyemura T (1960) Dielectric properties of woods as the indicator of the moisture. Bull Gov For Exp Sta 119:96–172
24. King AP (1950) The Radiation Characteristics of Conical Horn Antennas. Proc IRE 38:249–251
25. Schorr MG and Beck FJ (1950) Electromagnetic Field of the Conical Horn. J Appl Phys 21:795–801
26. Masuda M, Shimoda H, Tanaka K, Taguchi M (2001) Study on Dielectric Lens Antenna. Tech Report IEICE AP2000-178:41–46
27. Masuda M, Shimoda H, Tanaka K, Taguchi M (2002) Study on dielectric lens antenna —Part 2—. Tech Report IEICE AP2001-178:9–14

[Figure legends]

Fig. 1. A diffraction model of MMW during propagation through a specimen. $V_i(x, y)$, $f(x, y)$, and $g(x, y)$, complex amplitudes of an incident, a rectilinearly propagated, and a diffracted waves, respectively; $d\,\mathrm{Re}\sqrt{\bar{\varepsilon}}/2$ and l_0, distances of the diffraction areas in the specimen and air, respectively; $\varepsilon(x, y)$, complex permittivity distribution in the specimen; d and $\bar{\varepsilon}$, the thickness and averaged complex permittivity of the specimen, respectively.

Fig. 2. Experimental set-up for X-ray radiography of wood specimens.

Fig. 3. Relation of average attenuation, Γ, to product of average air-dry density, ρ_a, and thickness, d, for all specimens.

Fig. 4. Images of oven-dry density distributions in xy-plane for LT specimens.

Fig. 5. Images of oven-dry density distributions in xy-plane for LR specimens.

Fig. 6. Experimental setup of a MMW measurement system arranged in a right-handed Cartesian coordinate system (x, y, z). 1. Gunn diode (100 GHz), 2. Isolator, 3. Directional coupler, 4. PIN diode, 5. Phase shifter, 6. Conical horn antenna, 7. Teflon plano-parabolic lens, 8. Specimen, 9. Open-ended rectangular waveguide (inner cross section: $x \times y = 2.54 \times 1.27$ mm) covered with millimeter wave absorbent except open end, 10. Quadrature phase shifter, 11. Switching frequency generator (100 kHz), 12. Mixer, 13. Lock-in amplifier, 14. IQ-mixer, and 15. Dielectric waveguide. V_I and V_Q, output voltages of in-phase (I) and quadrature (Q) components of a MMW signal.

Fig. 7. Images of (a) amplitude, $|V_i|$, and (b) phase, $\arg V_i$, of incident wave at z = 110 mm, and (c) distributions of amplitude, $|V_0|$, and phase, $\arg V_0$, of wave without a specimen along x-axis at (y, z) = (0, 113 mm).

Fig. 8. Distributions of amplitude and phase of transmitted MMWs for LT specimens measured along x-axis at (y, z) = (0, 113 mm). V, measured complex amplitude; $g_s(x)$, complex amplitude estimated from a diffraction model.

Fig. 9. Distributions of amplitude and phase of transmitted MMWs for LR specimens measured along x-axis at (y, z) = (0, 113 mm). V, measured complex amplitude; $g_s(x)$, complex amplitude estimated from a diffraction model.

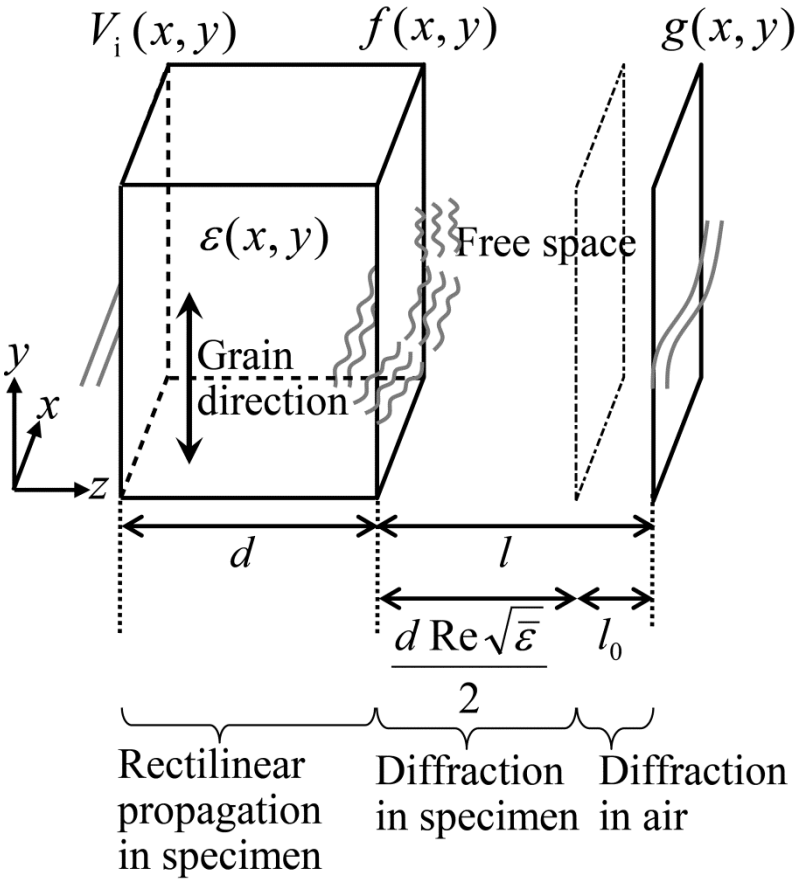
$V_i(x,y)$
$f(x,y)$
$g(x,y)$
$\varepsilon(x,y)$
Free space
Grain direction
y
x
z
d
l
$\frac{d\,\mathrm{Re}\sqrt{\bar{\varepsilon}}}{2}$
l_0
Rectilinear propagation in specimen
Diffraction in specimen
Diffraction in air

Fig. 1

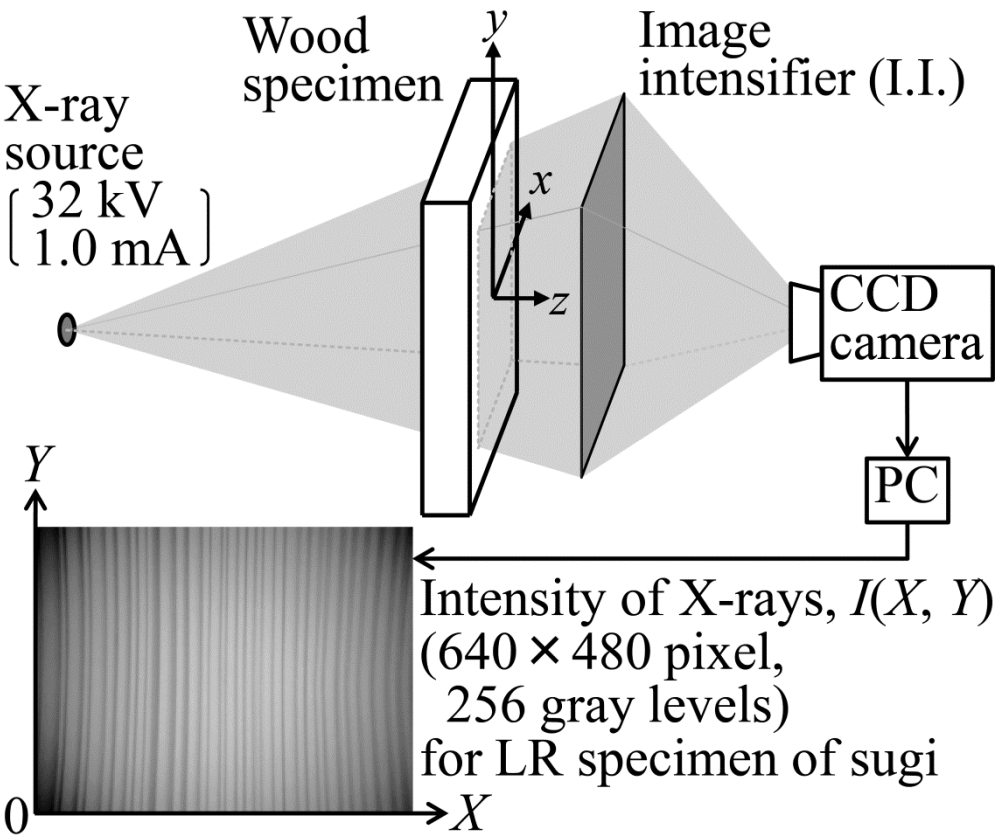
Wood
specimen
y
Image
intensifier (I.I.)
X-ray
source
32 kV
1.0 mA
x
z
CCD
camera
PC
Y
Intensity of X-rays, I(X, Y)
(640 × 480 pixel,
256 gray levels)
for LR specimen of sugi
0
X

Fig. 2

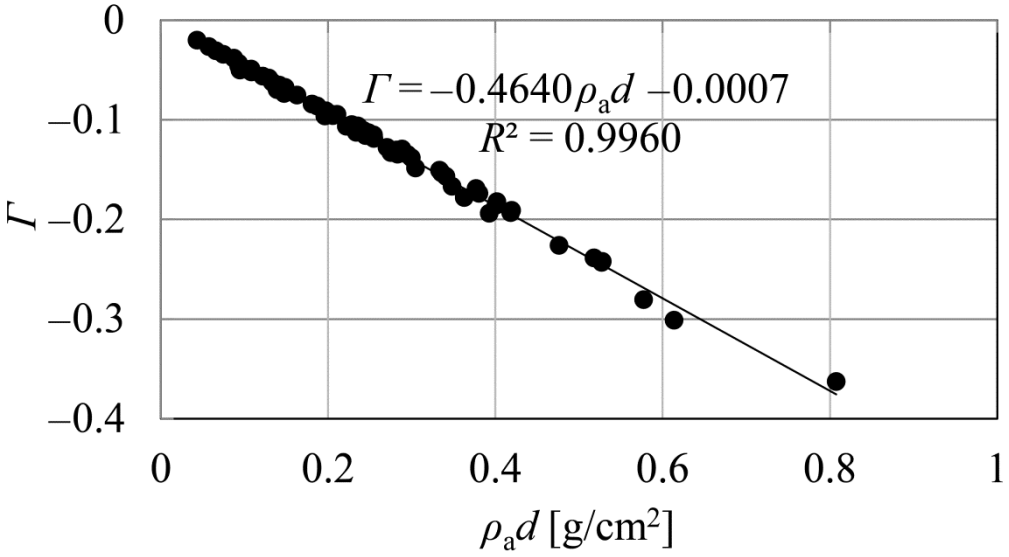

Fig. 3

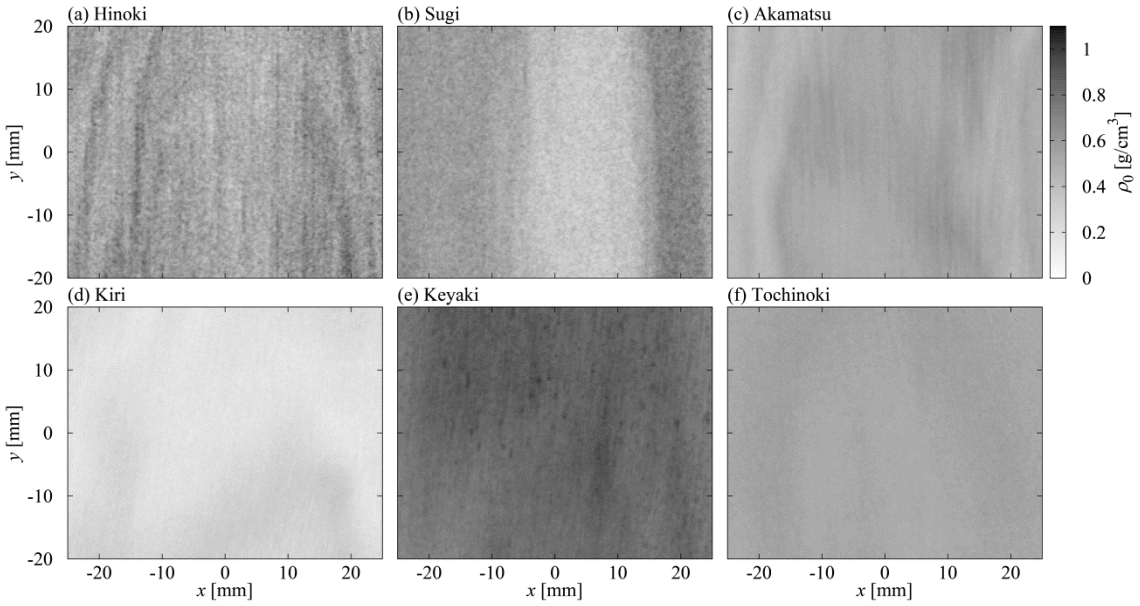
(a) Hinoki
(b) Sugi
(c) Akamatsu
(d) Kiri
(e) Keyaki
(f) Tochinoki
y [mm]
x [mm]
20
10
0
-10
-20
-20
-10
0
10
20
1
0.8
0.6
0.4
0.2
0
ρ0 [g/cm3]

Fig. 4

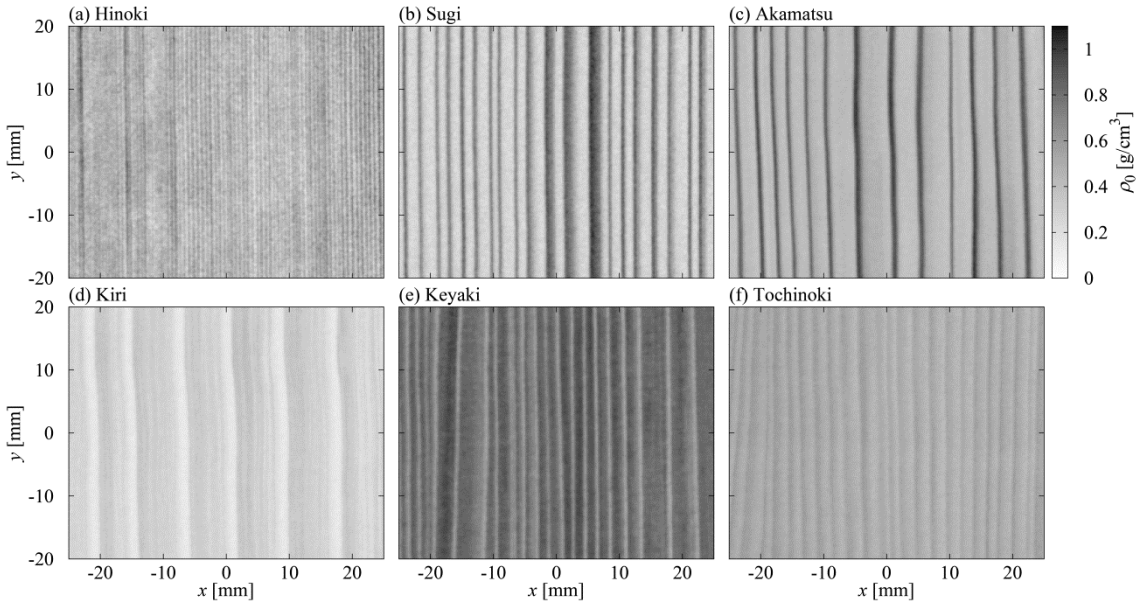
(a) Hinoki
(b) Sugi
(c) Akamatsu
(d) Kiri
(e) Keyaki
(f) Tochinoki
y [mm]
x [mm]
20
10
0
-10
-20
-20
-10
0
10
20
1
0.8
0.6
0.4
0.2
0
ρ0 [g/cm3]

Fig. 5

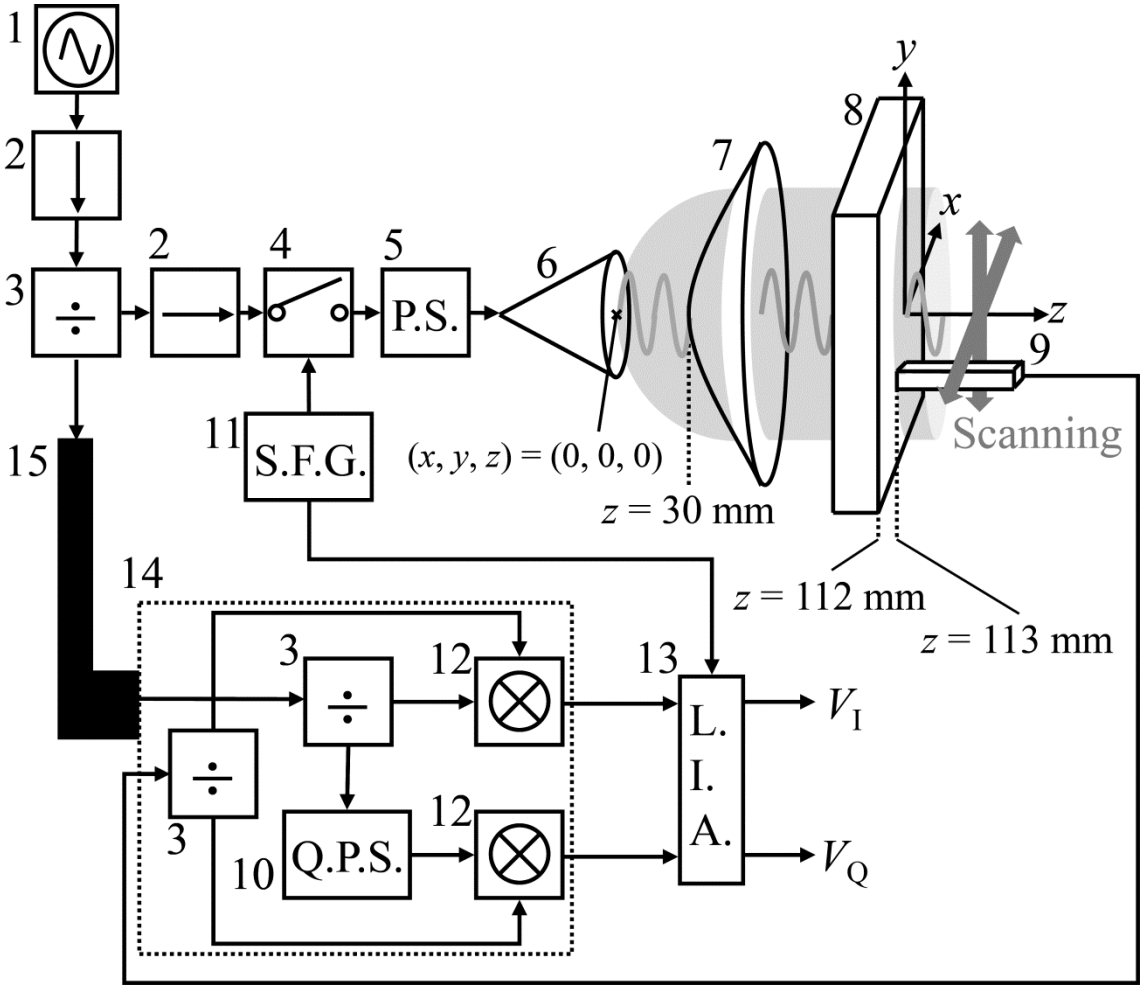
1
2
3
2
4
5
P.S.
6
7
8
y
x
z
9
Scanning
11
S.F.G.
15
(x, y, z) = (0, 0, 0)
z = 30 mm
z = 112 mm
z = 113 mm
14
3
12
13
L.
I.
A.
V_I
3
10
Q.P.S.
12
V_Q

Fig. 6

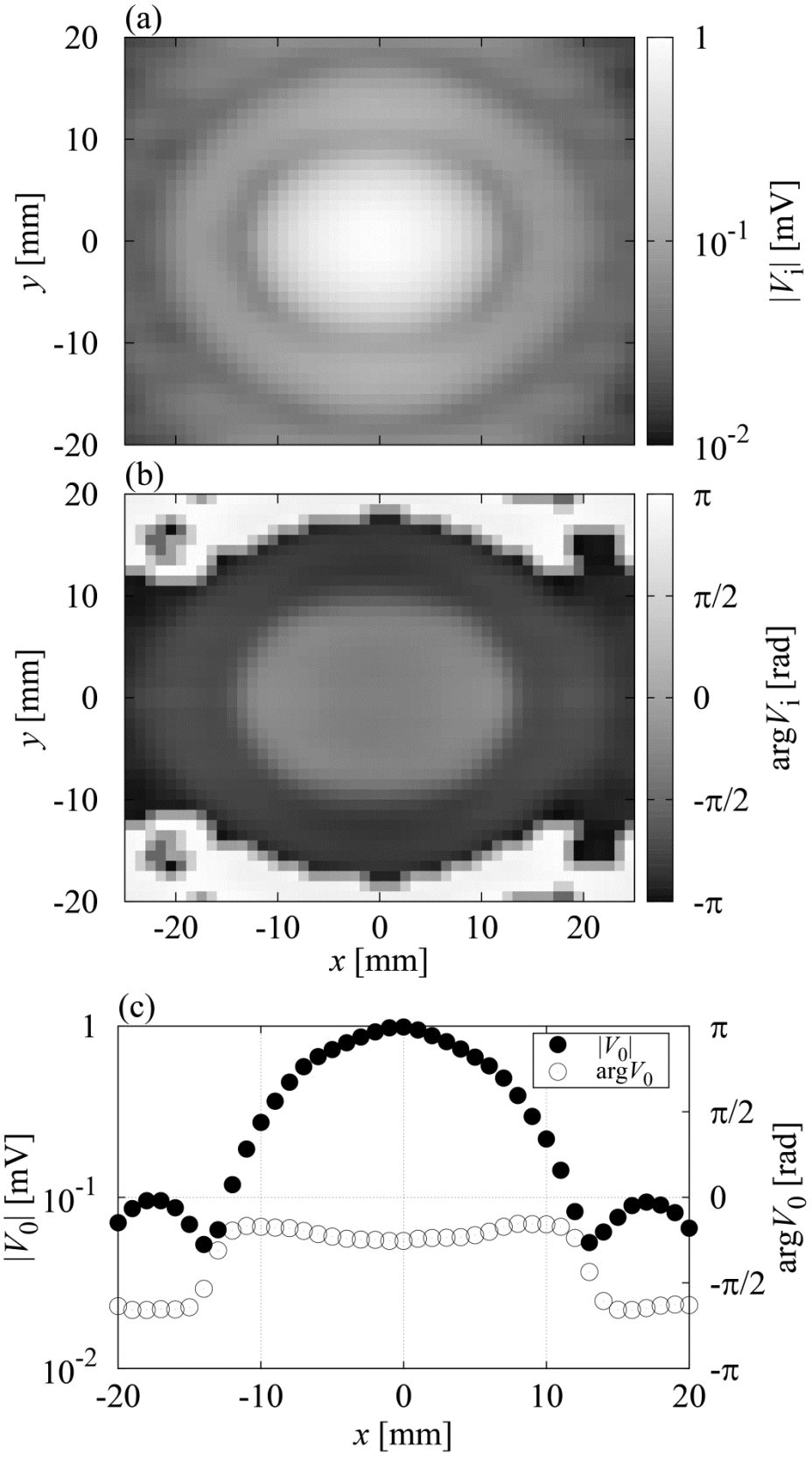
(a)
20
10
0
-10
-20
y [mm]
1
10^-1
10^-2
|V_i| [mV]
(b)
20
10
0
-10
-20
y [mm]
π
π/2
0
-π/2
-π
arg V_i [rad]
-20
-10
0
10
20
x [mm]
(c)
1
10^-1
10^-2
|V_0| [mV]
|V_0|
arg V_0
π
π/2
0
-π/2
-π
arg V_0 [rad]
-20
-10
0
10
20
x [mm]

Fig. 7

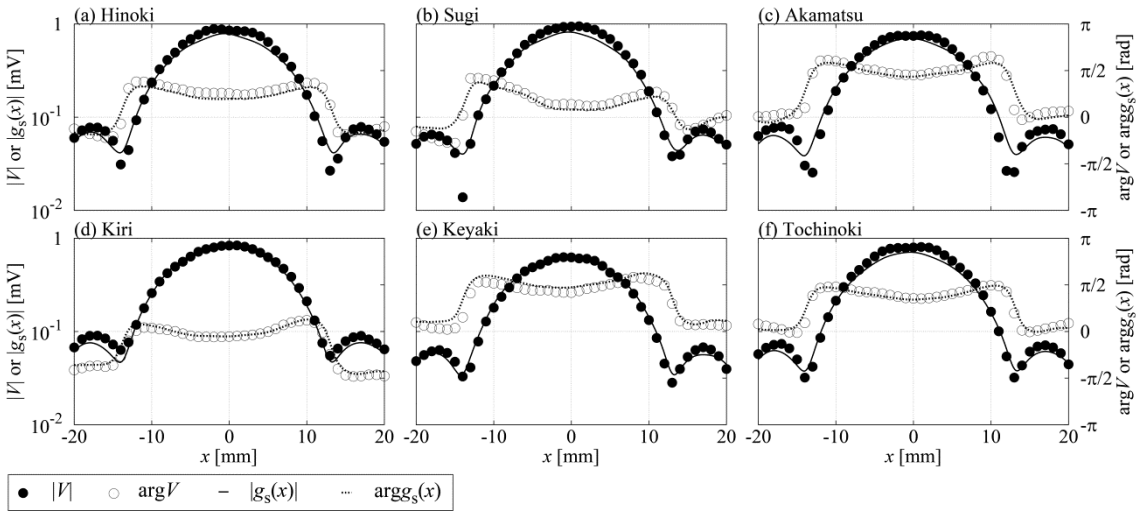
(a) Hinoki
(b) Sugi
(c) Akamatsu
(d) Kiri
(e) Keyaki
(f) Tochinoki
|V| or |g_s(x)| [mV]
arg V or arg g_s(x) [rad]
x [mm]
|V|
argV
|g_s(x)|
argg_s(x)

Fig. 8

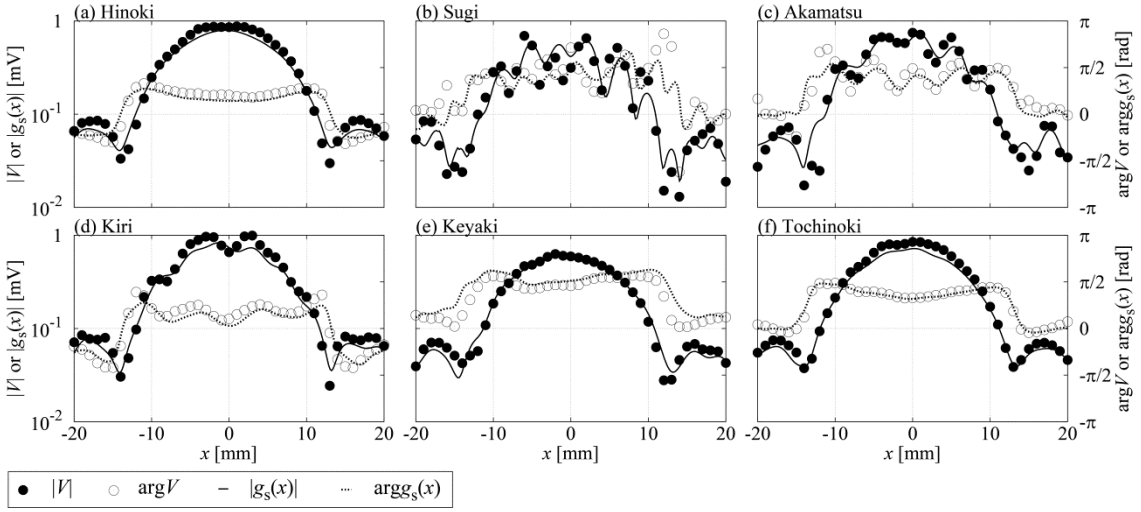
(a) Hinoki
(b) Sugi
(c) Akamatsu
(d) Kiri
(e) Keyaki
(f) Tochinoki
|V| or |g_s(x)| [mV]
arg V or arg g_s(x) [rad]
x [mm]
|V|
argV
|g_s(x)|
argg_s(x)

Fig. 9